



OPEN

SUBJECT AREAS:  
PHYSICS  
MATERIALS SCIENCEReceived  
14 September 2014Accepted  
16 December 2014Published  
20 January 2015Correspondence and  
requests for materials  
should be addressed to  
C.Y. (constantine.  
yannouleas@physics.  
gatech.edu)

# Interplay of relativistic and nonrelativistic transport in atomically precise segmented graphene nanoribbons

Constantine Yannouleas, Igor Romanovsky &amp; Uzi Landman

School of Physics, Georgia Institute of Technology, Atlanta, Georgia 30332-0430.

Graphene's isolation launched explorations of fundamental relativistic physics originating from the planar honeycomb lattice arrangement of the carbon atoms, and of potential technological applications in nanoscale electronics. Bottom-up fabricated atomically-precise segmented graphene nanoribbons, SGNRs, open avenues for studies of electrical transport, coherence, and interference effects in metallic, semiconducting, and mixed GNRs, with different edge terminations. Conceptual and practical understanding of electric transport through SGNRs is gained through nonequilibrium Green's function (NEGF) conductance calculations and a Dirac continuum model that absorbs the valence-to-conductance energy gaps as position-dependent masses, including topological-in-origin mass-barriers at the contacts between segments. The continuum model reproduces the NEGF results, including optical Dirac Fabry-Pérot (FP) equidistant oscillations for massless relativistic carriers in metallic armchair SGNRs, and an unequally-spaced FP pattern for mixed armchair-zigzag SGNRs where carriers transit from a relativistic (armchair) to a nonrelativistic (zigzag) regime. This provides a unifying framework for analysis of coherent transport phenomena and interpretation of forthcoming experiments in SGNRs.

Graphene, a single-atom-thin plane of graphite, has been the focus of intensive research endeavors since its isolation in 2004<sup>1</sup>. The high degree of interest in this material originates from its outstanding electronic, mechanical, and physical properties that result from the planar arrangement of the carbon atoms in a honeycomb lattice. Indeed graphene is considered both as a vehicle for exploring fundamental relativistic physics, as well as a promising material for potential technological applications in nanoscale electronics and optics<sup>2</sup>.

However, the absence of an electronic energy gap between the valence and conduction bands of 2D graphene casts doubts on its use in nanoelectronic devices. Nevertheless, theoretical studies had predicted that narrow graphene nanoribbons (GNRs) can have a large band gap, comparable to silicon ( $\sim 1$  eV), depending on the ribbon's width  $W$  and edge geometry (as well as possible doping at controlled positions). Pertinent to our work, we note that these predictions were made<sup>3-7</sup> for GNRs that have atomically precise armchair edges with widths  $W \leq 2$  nm. Consequently, the most recent advent and growing availability of bottom-up fabricated atomically-precise narrow graphene nanoribbons<sup>8-12</sup>, including segmented<sup>13</sup> armchair graphene nanoribbons (SaGNRs), opens promising avenues for graphene nanoelectronics and for detailed explorations of coherent electrical transport in nanoribbon-based graphene wires, nanoconstrictions, and quantum-point contacts.

Here we report on the unique aspects of transport through segmented GNRs obtained from tight-binding non-equilibrium Green's function<sup>14</sup> (TB-NEGF) calculations in conjunction with an analysis based on a one-dimensional (1D) relativistic Dirac model. This model is referred to by us as the Dirac-Fabry-Pérot (DFP) theory (see below for the choice of name). In particular, it is shown that the valence-to-conduction energy gap in armchair GNR (aGNR) segments, as well as the barriers at the interfaces between nanoribbon segments, can be incorporated in an effective position-dependent mass term in the Dirac hamiltonian; the transport solutions associated with this hamiltonian exhibit conductance patterns comparable to those obtained from the microscopic NEGF calculations. For zigzag graphene nanoribbon (zGNR) segments, the valence-to-conduction energy gap vanishes, and the mass term is consonant with excitations corresponding to massive nonrelativistic Schrödinger-type carriers.

As aforementioned, transport through narrow graphene channels – particularly bottom-up fabricated and atomically-precise graphene nanoribbons<sup>8-13</sup> – is expected to offer ingress to unique behavior of Dirac electrons in graphene nanostructures. In particular, the wave nature of elementary particles (e.g., electrons and photons) is commonly manifested and demonstrated in transport processes. Because of an exceptionally high electron



mobility and a long mean-free path<sup>1</sup>, it has been anticipated that graphene devices hold the promise for the realization, measurement, and possible utilization of fundamental aspects of coherent and ballistic transport behavior, which to date have been observed, with varying degrees of success, mainly at semiconductor interfaces<sup>15,16</sup>, quantum point contacts<sup>17</sup>, metallic wires<sup>18</sup>, and carbon nanotubes<sup>19</sup>. Prominent among the effects that accompany coherence and ballistic transport are conductance quantization (in nanoconstrictions) in steps of  $G_0 = 2e^2/h$ , which have been found earlier for quantum ballistic transport in semiconductor point contacts<sup>17</sup> and metal nanowires<sup>18</sup>. However, quantization signatures were scarcely observed<sup>20</sup> in GNRs fabricated with top-down methods.

Another manifestation of coherent ballistic transport are interference phenomena, reflecting the wave nature of the transporting physical object, and associated most often with optical (electromagnetic waves, photons) systems or with analogies to such systems (that is, the behavior of massless particles, as in graphene sheets). Measurements of interference patterns are commonly made with the use of interferometers, most familiar among them the multi-pass optical Fabry-Pérot (OFP) interferometer<sup>21</sup>, where the superposition of all the outgoing light waves, bouncing in a cavity from bounding partially reflecting mirrors, yields an oscillatory intensity record (interference pattern) which depends on the light wavelength and the distance between the mirrors.

The quest for demonstration of the particle-wave duality of electrons through measurement of quantum interference phenomena associated with electron transport in solid-state devices requires materials and configurations having long mean-free paths. This requirement limited early experimental work in the late 1980s to semiconductor heterostructures<sup>15,16</sup>, where conductance-quantization steps in gate-controlled two-dimensional constrictions have been observed. Subsequently interference patterns for nonrelativistic charge carriers in the form of conductance oscillations were observed<sup>22</sup> (and interpreted<sup>22,23</sup> as Fabry-Pérot-type phenomena) in semiconductor nanowires. The advent of 2D forms of carbon allotropes has motivated the study of optical-like interference phenomena associated with relativistic massless electrons, as in the case of metallic carbon nanotubes<sup>19</sup> and graphene 2D  $p$ - $n$  junctions<sup>24</sup>. (We note that the hallmark of the OFP is that the energy separation between successive maxima of the interference pattern varies as the inverse of the cavity length  $L$ .)

For GNRs with segments of different widths, our investigations reveal diverse transport modes beyond the OFP case, with conductance quantization steps ( $nG_0$ ,  $n = 1, 2, 3, \dots$ ) found only for uniform GNRs. In particular, three distinct categories of Fabry-Pérot interference patterns are identified:

1. *FP-A*: An optical FP pattern corresponding to massless graphene electrons exhibiting equal spacing between neighboring peaks. This pattern is associated with metallic armchair nanoribbon central segments. This category is subdivided further to *FP-A1* and *FP-A2* depending on whether a valence-to-conduction gap is absent (*FP-A1*, associated with metallic armchair leads), or present (*FP-A2*, corresponding to semiconducting armchair leads).
2. *FP-B*: A massive relativistic FP pattern exhibiting a shift in the conduction onset due to the valence-to-conduction gap and unequal peak spacings. This pattern is associated with semiconducting armchair nanoribbon central segments, irrespective of whether the leads are metallic armchair, semiconducting armchair, or zigzag.
3. *FP-C*: A massive non-relativistic FP pattern with  $1/L^2$  peak spacings, but with a vanishing valence-to-conduction gap,  $L$  being the length of the central segment. This pattern is the one expected for usual semiconductors described by the (nonrelativistic) Schrödinger equation, and it is associated with zigzag

nanoribbon central segments, irrespective of whether zigzag or metallic armchair leads are used.

The faithful reproduction of these unique TB-NEGF conductance patterns by the DFP theory, including mixed armchair-zigzag configurations (where the carriers transit from a relativistic to a non-relativistic regime), provides a unifying framework for analysis of coherent transport phenomena and for interpretation of experiments targeting fundamental understanding of transport in GNRs and the future development of graphene nanoelectronics.

## Results

**Segmented Armchair GNRs: All-metallic.** Our findings for the case of all-metallic<sup>3,7</sup> segmented aGNRs (when the number of carbons specifying the width is  $\mathcal{N}^W = 3l + 2$ ,  $l = 1, 2, 3, \dots$ ) are presented in Fig. 1; this lattice configuration is denoted as AAA (mmm). A uniform metallic armchair GNR [see Fig. 1(I)] exhibits ballistic quantized-conductance steps [see Fig. 1(a)]. In contrast, conductance quantization is absent for a nonuniform 3-segment aGNR; see Figs. 1(b) – 1(f). Instead of quantized steps, a finite number of oscillations appears, whose maxima (at the value of unity) maintain a constant energy separation. This behavior is indicative of optical-like Fabry-Pérot multiple reflections of the DW electron within the cavity defined by the two contacts (interfaces between the segments of different width). The patterns in Figs. 1(b) – 1(f) correspond to the category *FP-A1*.

The dependence of the conductance on the width of the leads relative to that of the constriction is explored by comparing the two junctions (exhibiting sharp lead-to-constriction interfaces) depicted in Fig. 1(II) and Fig. 1(III). Examination of the TB-NEGF conductances for these two segmented aGNRs [Fig. 1(c) and Fig. 1(e)] reveals that a wider lead [Fig. 1(III)] is associated with a stronger confinement (sharp conductance spikes) compared to a narrower lead [Fig. 1(II)] (oscillations). In the DFP results [Fig. 1(d) and Fig. 1(f)], which reproduce the TB-NEGF results, this trend is accounted for by varying the length and height of the mass barriers, which generates either a weak coupling (closed quantum-dot-like conductance spikes) or a strong coupling (open quantum-dot-like Fabry-Pérot-type oscillations) to the leads.

Further insight can be gained by an analysis of the discrete energies associated with the humps of the conductance oscillations in Fig. 1(c) and the resonant spikes in Fig. 1(e). Indeed a simplified approximation for the electron confinement in the continuum model consists in considering the graphene electrons as being trapped within a 1D infinite-mass square well (IMSW) of length  $L_1$  (the mass terms are infinite outside the interval  $L_1$  and the coupling to the leads vanishes). The discrete spectrum of the electrons in this case is given<sup>25</sup> by

$$E_n = \sqrt{\hbar^2 v_F^2 k_n^2 + \mathcal{M}^2 v_F^4}, \quad (1)$$

where the wave numbers  $k_n$  are solutions of the transcendental equation

$$\tan(k_n L_1) = -\hbar k_n / (\mathcal{M} v_F). \quad (2)$$

In the context of Fig. 1,  $\mathcal{M} = m_1 = 0$  (massless DW electrons), and one finds for the spectrum of the IMSW model:

$$E_n = (n + 1/2)\pi \hbar v_F / L_1, \quad (3)$$

with  $n = 0, 1, 2, \dots$ . Remarkably, the energies associated with the TB-NEGF oscillation humps and spikes in Figs. 1(c) and 1(e) [or Figs. 1(d) and 1(f) in the DFP model] follow very closely the above relation. Note the constant separation between successive energies,

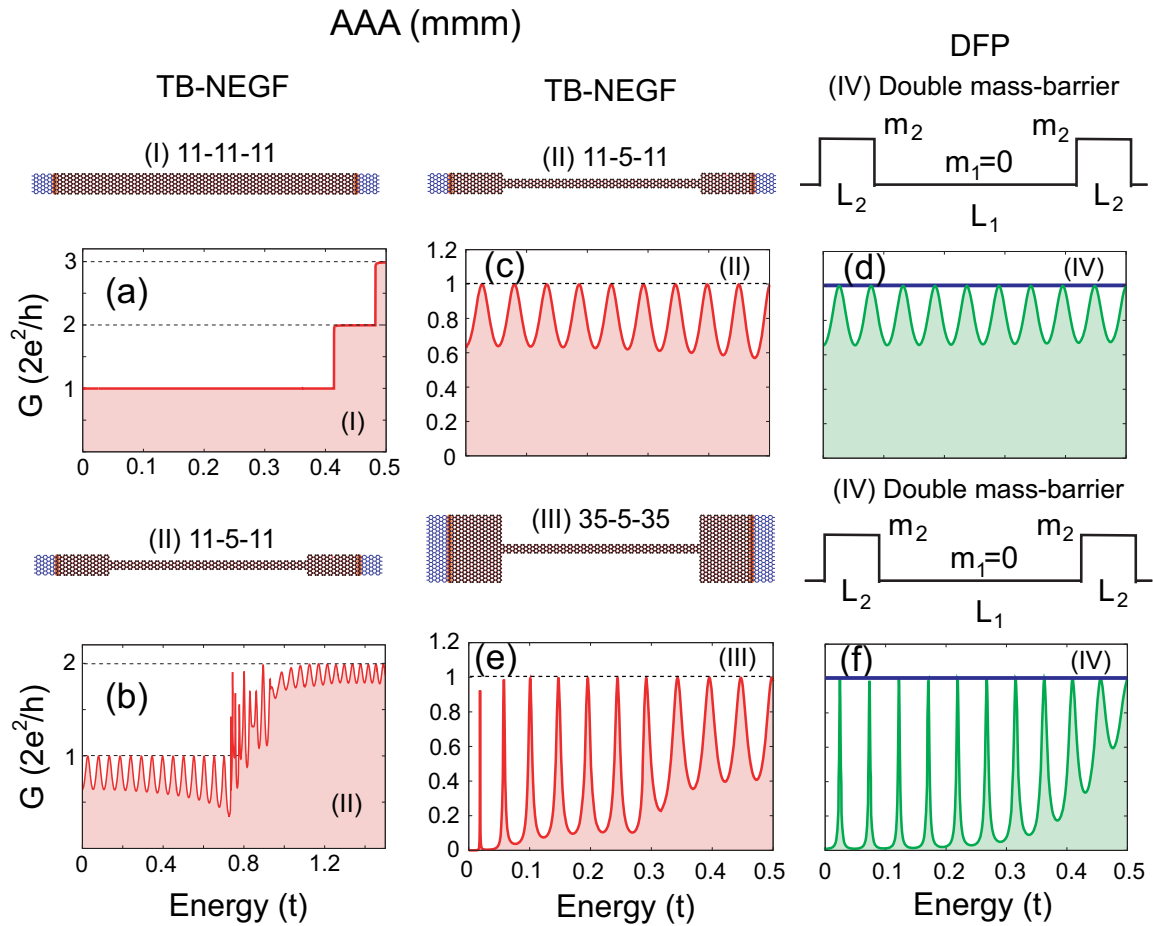


**Figure 1** | Conductance quantization steps (a) for a uniform metallic armchair nanoribbon (I) contrasted to Fabry-Pérot oscillations (b–f) for 3-segment all-metallic SaGNRs (II and III). The first two columns (employing red colors) display TB-NEGF results. The third column (employing green colors) displays continuum DFP results, which reproduce the TB-NEGF results in the middle column. (I–III) Schematics of the nanoribbons employed in the TB-NEGF calculations. A 3-segment segmented GNR is denoted as  $\mathcal{N}_1^W - \mathcal{N}_2^W - \mathcal{N}_3^W$ , with  $\mathcal{N}_i^W$  ( $i = 1, 2$ ) being the number of carbon atoms specifying the width of the ribbon segments. In all configurations, the semi-infinite leads are shown in blue color on the far left and far right. Note the steps  $nG_0$  in (a) reflecting full conductance quantization for the uniform nanoribbon. Instead of steps, the SaGNR junctions in (b–f) exhibit Fabry-Pérot-type conductance oscillations whose maxima are the places where conductance quantization is maintained. The effect of the relative widths of the leads and the constriction on the conductance of the all-metallic junctions is shown in (c,e) (TB-NEGF) and in (d,f) (corresponding DFP, respectively), illustrating Fabry-Pérot oscillations (c,d) for a constriction width close to that of the leads [see schematic (II)] and the development of a sharper oscillatory pattern [conductance spikes, see (e) and (f)] for a junction with much wider leads [see (III)]. The DFP approach is used to analyze the behavior of the TB-NEGF conductance in the energy range of the  $1G_0$  step [see (b)]. (IV) Diagram of the double mass-barrier used in the DFP method [case of massless Dirac-Weyl electrons with  $m_1 = 0$  and  $\mathcal{M}_l = 0$ ,  $\mathcal{M}_l$  being the carrier mass in the leads (not shown)]. The double-barrier parameters that reproduce the TB-NEGF results were  $L_1 = 58a_0$ ,  $L_2 = 1a_0$ ,  $m_2v_F^2 = t/3$  for (d) and  $L_1 = 60a_0$ ,  $L_2 = 6a_0$ ,  $m_2v_F^2 = t/4$  for (f). In the case of the wide leads (III), it is worth noting that the DFP theory reproduces the gradual widening of the spikes as a function of increasing energy; naturally this trend results from the weakening of the confinement effect due to a stronger coupling to the leads for higher energies. The horizontal solid lines at  $G = 1G_0$  (blue online) in (d) and (f) describe the DFP conductance obtained when employing a potential  $V(x)$  double barrier [similar in shape to the schematic in (IV)] and the assumption  $\phi(x) = 0$ ; the result is independent of the potential barrier's heights. In all figures (here and below), when a roman number is placed in the same frame along with a letter index, it indicates the corresponding lattice or DFP schematic specified by the roman number.  $a_0 = 0.246$  nm is the graphene lattice constant;  $t = 2.7$  eV is the hopping parameter.

$$E_n - E_{n-1} = 2E_0, \quad n = 1, 2, 3, \dots, \quad (4)$$

which is twice the energy

$$E_0 = \pi\hbar v_F / (2L_1) \quad (5)$$

of the lowest state.

As is well known, a constant energy separation of the intensity peaks, inversely proportional to the length of the resonating cavity [here  $L_1$ , see Eqs. (4) and (5) above] is the hallmark of the optical Fabry-Pérot, reflecting the linear energy dispersion of the photon in optics or a massless DW electron in graphene structures. For our

purpose, most revealing is the energy offset away from zero of the first conductance peak, which equals exactly one-half of the constant energy separation between the peaks. In onedimension, this is the hallmark of a massless fermion subject to an infinite-mass barrier confinement<sup>25</sup>, and it provides ultimate support for our introduction of mass barriers at the interfaces of the segmented aGNR. Naturally, in the case of a semiconducting segment (see below), this equidistant behavior and 1/2-offset of the conductance peaks do not apply; this case is accounted for by the Dirac-Fabry-Pérot model presented in Methods, and it is more general than the optical Fabry-Pérot theory associated with a photonic cavity<sup>21</sup>.

In the nonrelativistic limit, i.e., when  $\hbar k_n \ll \mathcal{M}v_F$ , one gets

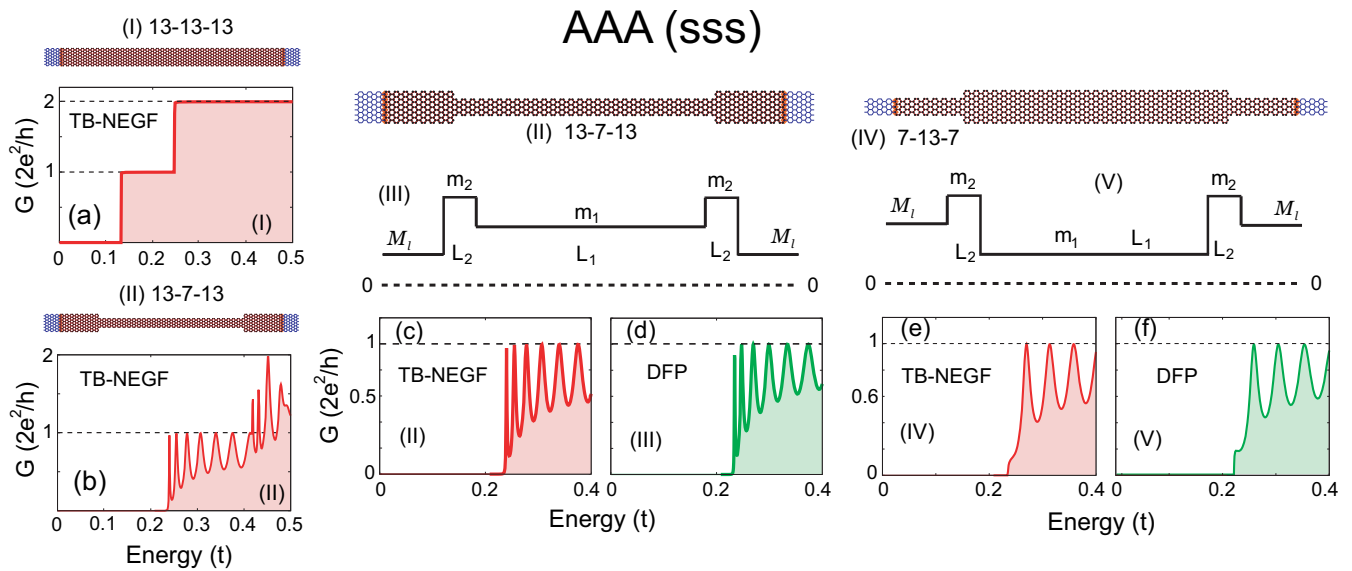


**Figure 2 | Conductance quantization steps (a) for a uniform semiconducting armchair nanoribbon (I) contrasted to Fabry-Pérot oscillations (b–f) of two 3-segment armchair GNRs [(II) and (IV)] with both a semiconducting central constriction and semiconducting leads (13-7-13 and 7-13-7). (III, V) Schematics of the mass barriers used in the DFP modeling, with the dashed line denoting the zero mass. The physics underlying such a junction is that of a massive relativistic Dirac fermion impinging upon the junction and performing multiple reflections (above  $m_1 v_F^2$ ) within a particle box defined by the double-mass barrier. (c,e) TB-NEGF conductance as a function of the Fermi energy of the *massive* Dirac electrons in the leads. (d) DFP conductance reproducing [in the energy range of the  $1G_0$  step, see (b)] the TB-NEGF result in (c). The mass-barrier parameters used in the DFP reproduction were  $L_1 = 55a_0$ ,  $m_1 v_F^2 = 0.22t$ ,  $L_2 = 1a_0$ ,  $m_2 v_F^2 = 0.5t$ . The mass of the electrons in the leads was  $\mathcal{M}_l v_F^2 = 0.166t$ . (f) DFP conductance reproducing the TB-NEGF result in (e). The parameters used in the DFP reproduction were  $L_1 = 53.6a_0$ ,  $m_1 v_F^2 = 0.166t$ ,  $L_2 = 1a_0$ ,  $m_2 v_F^2 = 0.51t$ . The mass of the electrons in the leads was  $\mathcal{M}_l v_F^2 = 0.22t$ .  $a_0 = 0.246$  nm is the graphene lattice constant;  $t = 2.7$  eV is the hopping parameter.**

$$\tan(k_n L_1) \sim 0, \quad (6)$$

which yields the well known relations  $k_n L_1 \sim n\pi$  and

$$E_n \sim \mathcal{M} v_F^2 + n^2 \hbar^2 \pi^2 / (2ML_1^2). \quad (7)$$

For a massive relativistic electron, as is the case with the semiconducting aGNRs in this paper, one has to numerically solve Eq. (2) and then substitute the corresponding value of  $k_n$  in Einstein's energy relation given by Eq. (1).

It is worth mentioning here that the inoperativeness for one-dimensional cases, due to Klein tunneling<sup>26</sup>, of the electrostatic potential  $V(x)$  [see horizontal blue lines at  $G = 1G_0$  in Figs. 1(d) and 1(f)] was also noted earlier; see the curves for normal incidence (labeled  $\theta = 0$ ) in Fig. 2 of Ref. 27.

**Segmented Armchair GNRs: All-semiconducting.** Our results for a 3-segment *all-semiconducting* aGNR are portrayed in Fig. 2 [see schematic lattice diagrams in Figs. 2(I) and 2(II)]; this lattice configuration is denoted as AAA (sss). A uniform semiconducting armchair GNR [see Fig. 2(I)] exhibits ballistic quantized-conductance steps [see Fig. 2(a)]. In contrast, conductance quantization is absent for a nonuniform 3-segment (13-7-13) aGNR; see Figs. 2(b)–2(d). Here, instead of quantized steps, oscillations appear as in the case of the all-metallic junctions presented earlier in Fig. 1. However, the first oscillation appears now at an energy  $\sim 0.22t$ , which reflects the intrinsic gap  $\Delta/2$  of the semiconducting central segment belonging to the class II of aGNRs, specified<sup>7,28</sup> by a width  $\mathcal{N}^W = 3l + 1$ ,  $l = 1, 2, 3, \dots$ . That the leads are semiconducting does not have any major effect. This is due to the fact that  $\mathcal{N}_2^W < \mathcal{N}_1^W$ , and as a result the energy gap  $m_1 v_F^2$  of

the central segment is larger than the energy gap  $\mathcal{M}_l v_F^2$  of the semiconducting leads [see schematic in Fig. 2(III)].

The armchair GNR case with interchanged widths (i.e., 7-13-7 instead of 13-7-13) is portrayed in Figs. 2(e)–2(f). In this case the energy gap of the semiconducting leads (being the largest) determines the onset of the conductance oscillations. It is a testimonial of the consistency of our DFP method that it can reproduce [see Fig. 2(d) and Fig. 2(f)] both the 13-7-13 and 7-13-7 TB-NEGF conductances; this is achieved with very similar sets of parameters taking into consideration the central-segment-leads interchange. We note that the larger spacing between peaks (and also the smaller number of peaks) in the 7-13-7 case is due to the smaller mass of the central segment (0.166  $t$  instead of 0.22  $t$ ).

From an inspection of Fig. 2, one can conclude that the physics associated with the all-semiconducting AAA junction is that of multiple reflections of a *massive* relativistic Dirac fermion bouncing back and forth from the edges of a particle box created by a double-mass barrier [see the schematic of the double-mass barrier in Fig. 2(III)]. In particular, to a good approximation the energies of the conductance oscillation peaks are given by the IMSW Eq. (2) with  $\mathcal{M} v_F^2 = m_1 v_F^2 = 0.22t$  (13-7-13) or  $\mathcal{M} v_F^2 = m_1 v_F^2 = 0.166t$  (7-13-7). In this respect, the separation energy between successive peaks in Figs. 2(b), 2(c), 2(e), and 2(f) is not a constant, unlike the case of the all-metallic junction.

The patterns in Figs. 2(c) and 2(f) correspond to the category *FP-B*. This generalized oscillations cannot be accounted for by the optical Fabry-Pérot theory, but they are well reproduced by the generalized Dirac-Fabry-Pérot model introduced by us in the Methods.

**Segmented Armchair GNRs: semiconducting-metallic-semiconducting.** Our results for a 3-segment (7-5-7) *semiconducting-metallic-semiconducting* aGNR are portrayed in Fig. 3 [see schematic lattice diagram in Fig. 3(I)]; this lattice configuration is denoted as AAA (sms). The first FP oscillation in the TB-NEGF conductance

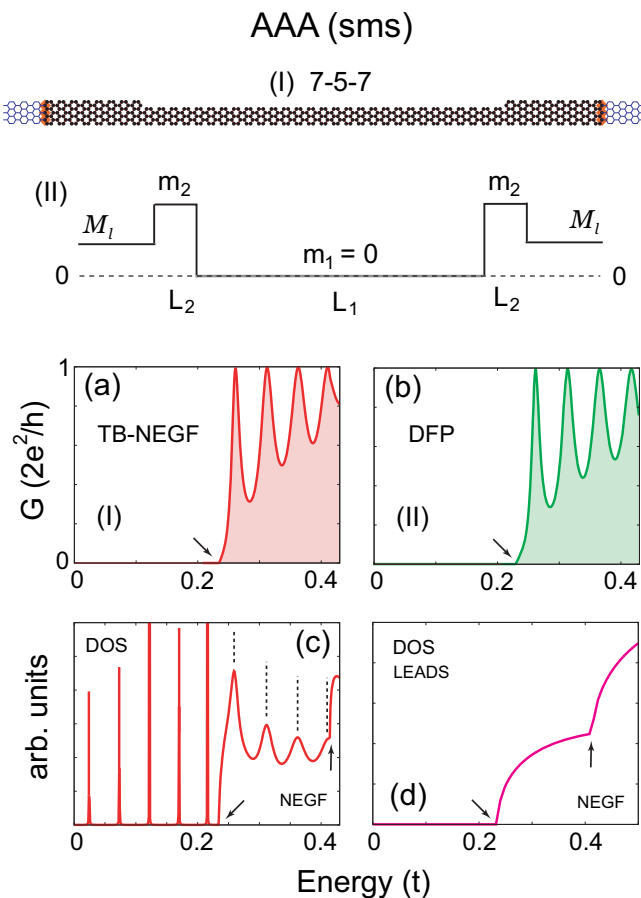


**Figure 3 | Conductance for a 3-segment nanoribbon with a metallic ( $\mathcal{N}_2^W = 5$ ) central constriction and semiconducting leads ( $\mathcal{N}_1^W = 7$ ).** The semi-infinite leads (in blue on the far left and far right) are an extension of the left and right semiconducting segments with  $\mathcal{N}_1^W = 7$ ; see schematic lattice diagram in (I). (II) Schematics of the mass barriers used in the DFP modeling, with the dashed line denoting the zero mass. The physics underlying such a junction is that of a massive relativistic Dirac fermion impinging upon the junction, which loses its mass upon tunneling in the central segment and performs multiple reflections within a particle box defined by the double-mass barrier. (a) TB-NEGF conductance as a function of the Fermi energy of the massive Dirac electrons in the leads. (b) DFP conductance reproducing the TB-NEGF result in (a). The mass-barrier parameters used in the DFP reproduction were  $L_1 = 60.4a_0$ ,  $m_1 = 0$ ,  $L_2 = 1a_0$ ,  $m_2v_F^2 = 0.37t$ . The mass of the electrons in the leads was  $\mathcal{M}_1v_F^2 = 0.23t$ . (c) – (d) The total DOS of the junction and the density of states in the isolated leads, respectively, according to the TB-NEGF calculations. The arrows indicate the onset of the electronic bands in the leads. Note that the DOS in (c) reveal the existence of five sharp electronic states below the onset (at  $0.23t \equiv \mathcal{M}_1v_F^2$ ) of the first band in the leads [see (d)], which consequently do not generate any conductance resonances [see (a) and (b)]. Note further in (c) the equal energy spacing between the vertical lines [the five solid (red) and four dashed (black) ones] associated with the resonances of a massless electron confined within the central metallic aGNR segment.  $a_0 = 0.246$  nm is the graphene lattice constant;  $t = 2.7$  eV is the hopping parameter.

displayed in Fig. 3(a) appears at an energy  $\sim 0.23 t$ , which reflects the intrinsic gap  $\Delta/2$  of the semiconducting leads (with  $\mathcal{N}_1^W = 7$ ). The energy spacing between the peaks in Fig. 3(a) is constant in agreement with the metallic (massless DW electrons) character of the central segment with  $\mathcal{N}_2^W = 5$ . The TB-NEGF pattern in Fig. 3(a) corresponds to the Fabry-Pérot category *FP-A2*. As seen from

Fig. 3(b), our generalized Dirac-Fabry-Pérot theory is again capable of faithfully reproducing this behavior.

A deeper understanding of the AAA (sms) case can be gained via an inspection of the density of states (DOS) plotted in Fig. 3(c) for the total segmented aGNR (central segment plus leads) and in Fig. 3(d) for the isolated leads. In Fig. 3(c), nine equidistant resonance lines are seen. Their energies are close to those resulting from the IMSW Eq. (3) (with  $L_1 = 60.4a_0$ , see the caption of Fig. 3) for a massless DW electron. Out of these nine resonances, the first five do not conduct [compare Figs. 3(a) and 3(c)] because their energies are lower than the minimum energy (i.e.,  $\Delta/2 = \mathcal{M}_1v_F^2 \sim 0.23t$ ) of the incoming electrons in the leads [see the onset of the first band (marked by an arrow) in the DOS curve displayed in Fig. 3(d)].

**Segmented Armchair GNRs: Effects of hydrogen passivation.** As shown in Refs. 4, 5, a detailed description of hydrogen passivation requires that the hopping parameters  $t'$  for the nearest-neighbor C-C bonds at the armchair edges be given by  $t' = 1.12 t$ . Taking this modification into account, our results for a 3-segment *semiconducting-metallic-semiconducting* aGNR are portrayed in Fig. 4 [see schematic lattice diagram in Fig. 4(I)]; this lattice configuration is denoted as “AAA (sms) H-passivation.” The first FP oscillation in the TB-NEGF conductance displayed in Fig. 4(a) appears at an energy  $\sim 0.28 t$ , which reflects the intrinsic gap  $\Delta/2$  of the properly passivated semiconducting leads (with  $\mathcal{N}_1^W = 7$ ). The energy spacing between the peaks in Fig. 4(a) is slightly away from being constant in agreement with the small mass  $m_1v_F^2 = 0.05t$  acquired by the central segment with  $\mathcal{N}_2^W = 5$ , due to taking  $t' = 1.12 t$ . As seen from Fig. 4(b), our generalized Dirac-Fabry-Pérot theory is again capable of faithfully reproducing this behavior.

A deeper understanding of the AAA (sms)-H-passivation case can be gained via an inspection of the DOS plotted in Fig. 4(c) for the total segmented aGNR (central segment plus leads) and in Fig. 4(d) for the isolated leads. In Fig. 4(c), eight (almost, but not exactly, equidistant) resonance lines are seen. Their energies are close to those resulting from the IMSW Eq. (2) (with  $L_1 = 59.5a_0$  and  $m_1v_F^2 = 0.05t$ ; see the caption of Fig. 4) for a Dirac electron with a small mass. Out of these eight resonances, the first six do not conduct [compare Figs. 4(a) and 4(c)] because their energies are lower than the minimum energy (i.e.,  $\Delta/2 = \mathcal{M}_1v_F^2 \sim 0.28t$ ) of the incoming electrons in the leads [see the onset of the first band (marked by an arrow) in the DOS curve displayed in Fig. 4(d)]. From the above we conclude that hydrogen passivation of the aGNR resulted in a small shift of the location of the states, and opening of a small gap for the central metallic narrower (with a width of  $\mathcal{N}_2^W = 5$ ) segment, but did not modify the conductance record in any qualitative way. Moreover, the passivation effect can be faithfully captured by the Dirac FP model by a small readjustment of the model parameters.

**All-zigzag segmented GNRs.** It is interesting to investigate the sensitivity of the interference features on the edge morphology. We show in this section that the relativistic transport treatment applied to segmented armchair GNRs does not maintain for the case of a nanoribbon segment with zigzag edge terminations. In fact zigzag GNR (zGNR) segments exhibit properties akin to the well-known transport in usual semiconductors, i.e., their excitations are governed by the nonrelativistic Schrödinger equation.

Before discussing segmented GNRs with zigzag edge terminations, we remark that such GNRs with uniform width exhibit stepwise quantization of the conductance, similar to the case of a uniform metallic armchair-edge-terminated GNR [see Fig. 2(a)].

In Fig. 5(a), we display the conductance in a three-segment junction [see lattice schematic in Fig. 5(I)] when all three segments have zigzag edge terminations (denoted as ZZZ). The main finding is that the central segment behaves again as a resonant cavity that yields an oscillatory conductance pattern where the peak spacings are unequal

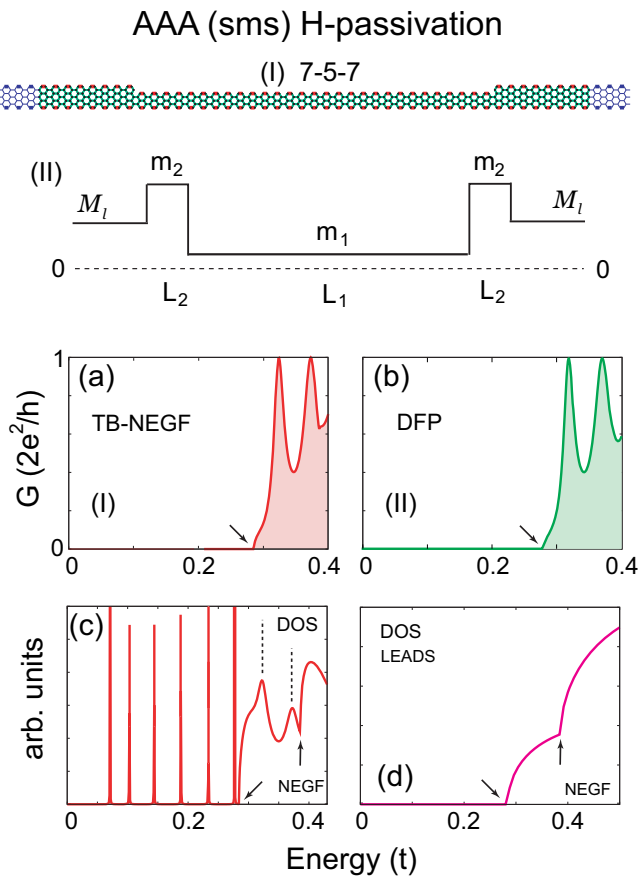


**Figure 4 | H-passivation effects in the conductance of a 3-segment armchair nanoribbon with a metallic ( $\mathcal{N}_2^W = 5$ ) central constriction and semiconducting leads ( $\mathcal{N}_1^W = 7$ ); see schematic lattice diagram in (I).** Note that the nearest-neighbor C-C bonds at the armchair edges (thick red and blue lines) have hopping parameters  $t' = 1.12 t$ . (II) Schematics of the position-dependent mass field used in the DFP modeling, with the dashed line denoting the zero mass. The physics underlying such a junction is that of a massive relativistic Dirac fermion impinging upon the junction, which reduces its mass close to zero upon tunneling in the central segment and performs multiple reflections within a particle box defined by the double-mass barrier. (a) TB-NEGF conductance as a function of the Fermi energy. (b) DFP conductance reproducing the TB-NEGF result in (a). The mass parameters used in the DFP reproduction were  $L_1 = 59.5a_0$ ,  $m_1v_F^2 = 0.05t$ ,  $L_2 = 1.5a_0$ ,  $m_2v_F^2 = 0.30t$ . The mass of the electrons in the leads was  $\mathcal{M}_1v_F^2 = 0.28t$ . (c) – (d) The total DOS of the junction and the density of states in the isolated leads, respectively, according to the TB-NEGF calculations. The arrows indicate the onset of the electronic bands in the leads; note the shifts from  $0.23 t$  to  $0.28 t$  and from  $0.42 t$  to  $0.38 t$  for the onsets of the first and second bands, respectively, compared to the case with  $t' = t$  in Fig. 3(d). Compared to Fig. 3, the subtle modifications of mass parameters brought about by having  $t' = 1.12 t$  result in having six sharp electronic states [see (c)] below the onset (at  $0.28t \equiv \mathcal{M}_1v_F^2$ ) of the first band in the leads [see (d)], which consequently do not generate any conductance resonances [see (a) and (b)]. In addition, within the energy range ( $0$  to  $0.4 t$ ) shown in (a) and (b), there are now only two conducting resonances, instead of three compared to Figs. 3(a) and 3(b).  $a_0 = 0.246$  nm is the graphene lattice constant;  $t = 2.7$  eV is the graphene hopping parameter.

[Fig. 5(a)]. This feature, which deviates from the optical Fabry-Pérot behavior, appeared also in the DFP patterns for a three-segment armchair junction whose central segment was semiconducting, albeit with a different dependence on  $L$  [see Figs. 2 and Eq. (2)]. Moreover, from a set of systematic calculations (not shown) employing different

lengths and widths, we found that the energy of the resonant levels in zGNR segments varies on the average as  $\sim (n/L)^2$ , where the integer  $n$  counts the resonances and  $L$  indicates the length of the central segment. However, a determining difference with the armchair GNR case in Fig. 2 is the vanishing of the valence-to-conductance gap in the zigzag case of Fig. 5(a). It is well known that the above features are associated with resonant transport of electronic excitations that obey the second-order nonrelativistic Schrödinger equation.

Naturally, one could formulate a continuum transport theory based on transfer matrices (see Methods) that use the 1D Schrödinger equation instead of the generalized Dirac Eq. (8). Such a Schrödinger-equation continuum approach, however, is unable to describe mixed armchair-zigzag interfaces (see below),

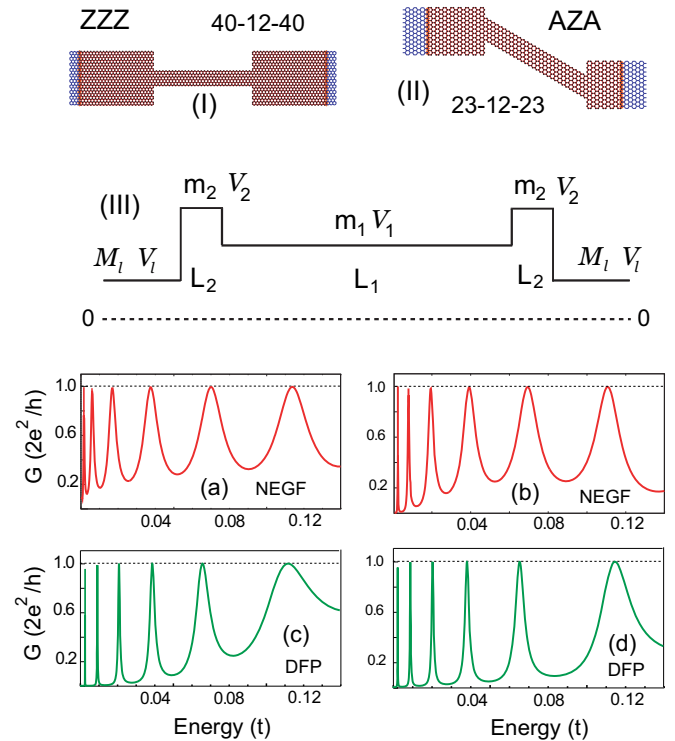


**Figure 5 | Conductance for ZZZ (all-zigzag, left column) and AZA (armchair-zigzag-armchair, right column) segmented nanoribbon junctions.** See corresponding lattice diagrams in (I) and (II). The 3-segment GNRs are denoted as  $\mathcal{N}_1^W - \mathcal{N}_2^W - \mathcal{N}_1^W$ , with  $\mathcal{N}_i^W$  ( $i = 1, 2$ ) being the number of carbon atoms specifying the width of the ribbon segments. The armchair leads in the AZA junction are metallic ( $\mathcal{N}_1^W = 23$ , class III aGNR). (a) – (b) TB-NEGF conductance for the ZZZ and AZA junction, respectively. (c) DFP conductance reproducing the TB-NEGF result in (a) for the ZZZ junction. (d) DFP conductance reproducing the TB-NEGF result in (b) for the AZA junction. In spite of the different edge morphology, the Fabry-Pérot patterns in (a) and (b) are very similar. The central zigzag segment controls the Fabry-Pérot patterns. According to the continuum DFP analysis, the physics underlying such patterns is that of a massive nonrelativistic Schrödinger fermionic carrier performing multiple reflections within a cavity defined by a double-mass barrier [see diagram in (III)], but with the additional feature that  $V_1 = -m_1v_F^2$  and  $V_2 = -\mathcal{M}_1v_F^2$  are also considered for segments or leads with zigzag edge terminations (see text for details). The mass and  $V_i$  parameters used in the DFP calculations were  $L_1 = 30a_0$ ,  $m_1v_F^2 = 2.23t - cEt$ , with  $c = 7.3$ ,  $V_1 = -m_1v_F^2$ ,  $L_2 = 1.1a_0$ ,  $m_2v_F^2 = 0.38t$ ,  $V_2 = -m_2v_F^2/3$ ,  $\mathcal{M}_1v_F^2 = 2.30t$ ,  $V_1 = -\mathcal{M}_1v_F^2$  in (c) and  $L_1 = 29.1a_0$ ,  $m_1v_F^2 = 2.65t - cEt$ , with  $c = 8.4$ ,  $V_1 = -m_1v_F^2$ ,  $L_2 = 1.0a_0$ ,  $m_2v_F^2 = 0.30t$ ,  $V_2 = -m_2v_F^2$ ,  $\mathcal{M}_1 = 0$ ,  $V_1 = 0$  in (d).  $\mathcal{M}_1$  and  $V_i$  denote parameters of the leads.  $E$  is the energy in units of  $t$ .  $a_0 = 0.246$  nm is the graphene lattice constant;  $t = 2.7$  eV is the hopping parameter.



where the electron transits between two extreme regimes, i.e., an ultrarelativistic (i.e., including the limit of vanishing carrier mass) Dirac regime (armchair segment) and a nonrelativistic Schrödinger regime (zigzag segment). We have thus been led to adopt the same Dirac-type transfer-matrix approach as with the armchair GNRs, but with nonvanishing potentials  $V = \eta \mathcal{M} v_F^2$ , with  $\eta = \Theta(-E) - \Theta(E)$ , where  $\Theta(E)$  is the Heaviside step function. This amounts to shifts (in opposite senses) of the energy scales for particle and hole excitations, respectively, and it yields the desired vanishing value for the valence-to-conduction gap of a zigzag GNR.

The calculated DFP conductance that reproduces well the TB-NEGF result for the ZZZ junction [Fig. 5(a)] is displayed in Fig. 5(c); the parameters used in the DFP calculation are given in the caption of Fig. 5. We note that the carrier mass ( $m_1$ ) in the central zigzag segment exhibits an energy dependence. This is similar to a well known effect (due to nonparabolicity in the  $E - k$  dispersion) in the transport theory of usual semiconductors<sup>29</sup>. We further note that the average mass associated with a zigzag segment is an order of magnitude larger than that found for semiconducting armchair segments of similar width (see captions in Fig. 2, and this yields energy levels  $\sim (n/L)^2$  close to the nonrelativistic limit [see Eq. (7)]. We note that FP pattern of the ZZZ junction belongs to the category *FP-C*.

**Mixed armchair-zigzag-armchair segmented GNRs.** Fig. 5 (right column) presents an example of a mixed armchair-zigzag-armchair (AZA) junction, where the central segment has again zigzag edge terminations [see lattice schematic in Fig. 5(II)]. The corresponding TB-NEGF conductance is displayed in Fig. 5(b). In spite of the different morphology of the edges between the leads (armchair) and the central segment (zigzag), the conductance profile of the AZA junction [Fig. 5(b)] is very similar to that of the ZZZ junction [Fig. 5(a)]. This means that the characteristics of the transport are determined mainly by the central segment, with the left and right leads, whether zigzag or armchair, acting as reservoirs supplying the impinging electrons.

The DFP result reproducing the TB-NEGF conductance is displayed in Fig. 5(d), and the parameters used are given in the caption. We stress that the mixed AZA junction represents a rather unusual physical regime, where an ultrarelativistic Dirac-Weyl massless electron (due to the metallic armchair GNRs in the leads) transits to a nonrelativistic massive Schrödinger one in the central segment. We note that FP pattern of the AZA junction belongs to the category *FP-C*.

**Mixed zigzag-armchair-zigzag segmented GNRs.** Finally Fig. 6 presents an example of a mixed zigzag-armchair-zigzag (ZAZ) junction, where the central segment corresponds to a metallic armchair GNR [see lattice schematic in Fig. 6(I)]. The corresponding TB-NEGF conductance is displayed in Fig. 6(a). In spite of the different morphology of the edges between the leads (zigzag) and the central segment (armchair), the conductance profile of the ZAZ junction [Fig. 6(a)] is controlled by determined the central segment, with the left and right leads acting as reservoirs supplying the impinging electrons. Thus the conductance peaks are close to being equidistant, and the FP pattern belongs to the category *FP-A1*. The DFP result reproducing the TB-NEGF conductance is displayed in Fig. 6(b), and the parameters used are given in the caption.

In a reverse sense compared to the AZA junction above, the mixed ZAZ junction here represents also a rather unique physical regime, where a nonrelativistic massive Schrödinger electron (due to the zigzag GNRs in the leads) transits to an ultrarelativistic Dirac-Weyl massless one in the central segment. The decisive advances brought forward by our DFP 1D continuum theory can be clearly appreciated by its ability to describe the corresponding TB-NEGF results for these highly nontrivial ZAZ and AZA junctions [compare Figs. 6(a) and 6(b), as well as Figs. 5(b) and 5(d)]. Continuum 2D

formulations are unable to describe the important all-zigzag and mixed armchair/zigzag junctions described in this section, because they cannot distinguish between armchair and zigzag edges.

## Discussion

To motivate the 1D Dirac formalism developed and utilized here, we note that customarily armchair or zigzag edge terminations in two-dimensional (2D) graphene nanoribbons are treated with the massless 2D Dirac equation with the use of the corresponding boundary conditions<sup>30</sup>. In our study, however, narrow GNRs are treated with a 1D generalized Dirac equation. This approach is reminiscent of the 1D description of GNRs as described in Ref. 31 and also reviewed in Ref. 7, where the tight-binding 2D spectrum is projected onto the longitudinal wavenumber direction,  $k_x$ . For the armchair case (see Eqs. 10 on Ref. 31), the low-energy range of the 1D spectrum can be well approximated by the Einstein energy relation with a non-zero mass term for the semiconducting case, and with a zero mass term for the metallic case which exhibits a massless linear dependence (photon-like dispersion) of the energy on the momentum.

As a function of  $k_x$ , the zigzag GNRs exhibit a partially at  $E \sim 0$  band due to the localized (in the transverse direction) edge state. The

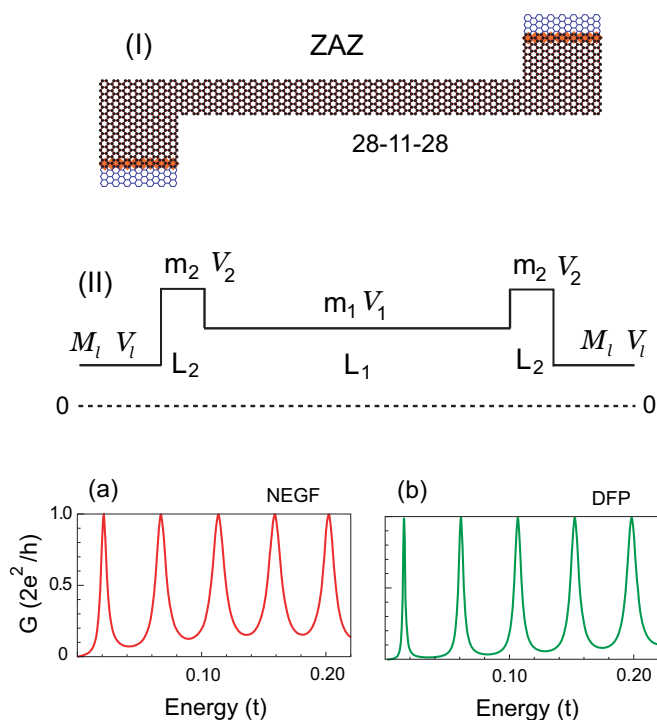


**Figure 6 | Conductance for a ZAZ (zigzag-armchair-zigzag) segmented nanoribbon junction.** See corresponding lattice diagram in (I). The 3-segment GNRs are denoted as  $\mathcal{N}_1^W - \mathcal{N}_2^W - \mathcal{N}_1^W$ , with  $\mathcal{N}_i^W$  ( $i=1,2$ ) being the number of carbon atoms specifying the width of the ribbon segments. The central armchair segment in the ZAZ junction is metallic ( $\mathcal{N}_2^W = 11$ , class III aGNR). (a) TB-NEGF conductance for the ZAZ junction. (b) DFP conductance reproducing the TB-NEGF result in (a) for the ZAZ junction. The central armchair segment controls the Fabry-Pérot patterns. According to the continuum DFP analysis, the physics underlying such patterns is that of a massless relativistic Dirac-Weyl fermionic carrier performing multiple reflections within a cavity defined by a double-mass barrier [see diagram in (II)], but with the additional feature that  $V_i = -\mathcal{M}_i v_F^2$  are also considered for the leads with zigzag edge terminations (see text for details). The mass and  $V_i$  parameters used in the DFP calculations were  $L_1 = 66a_0$ ,  $m_1 = 0$ ,  $V_1 = 0$ ,  $L_2 = 1a_0$ ,  $m_2 v_F^2 = 0.50t$ ,  $V_2 = 0$ ,  $\mathcal{M}_1 v_F^2 = 2t$ ,  $V_i = -\mathcal{M}_i v_F^2$ .  $E$  is the energy in units of  $t$ .  $a_0 = 0.246$  nm is the graphene lattice constant;  $t = 2.7$  eV is the hopping parameter.



at part is centered around  $k_x = \pi$  (alternatively taken as  $k_x = 0$  in Ref. 30), where  $E(k_x = \pi) = 0$ , and it expands towards the graphene Dirac points located at  $2\pi/3$  (alternatively,  $k_x = -\pi/3$ ) and  $4\pi/3$  (alternatively  $k_x = \pi/3$ ) as the width of the ribbon increases (see Fig. 7 in Ref. 7). After reaching the ends of the at part, the energy band opens two branches with non-zero energies; these branches do not have a linear dependence on  $k_x$ . Although this can be termed also as a “gapless” spectrum (like the metallic armchair case), the two differ in their dispersion relation – that is the energy of the former (zigzag) is approximately independent of the momentum for a broad range of the  $k_x$  momentum (see examples for various widths of zigzag GNRs in Fig. 4 of Ref. 7), whereas the latter (armchair) shows a linear energy-momentum relationship (see Fig. 3 in Ref. 7).

As the width of the GNRs get smaller (narrow zigzag nanoribbons), the range of the aforementioned at part decreases, and in the limit of a single row of benzene rings (the narrow-most zigzag GNR, referred to as polyacene) the dispersion curve transforms<sup>32</sup> into two (electron-hole) parabolas touching at  $k_x = \pi$ . The spectrum of polyacene is gapless, but due to the nonrelativistic parabolic dispersion, a mass,  $\mathcal{M}$ , is associated<sup>32</sup> with the second derivative according to the nonrelativistic relation  $p^2/2\mathcal{M}$ . The case of narrow zigzag GNRs that we study here is closer to the nonrelativistic polyacene than to the relativistic massless graphene (i.e., the limit of a zigzag ribbon of infinite width). Incidentally, we mention that the polyacene parabolic-band limit is not obtained<sup>33</sup> through a treatment employing the massless 2D Dirac equation with boundary conditions.

We comment here that physical circumstances where a change in some system configuration can result in a change in the nature of the dispersion relation (e.g from linear to quadratic), are not that rare. Another example is found when comparing the gapless, but linear in momentum, dispersion of the energy of particles (massless relativistic) in a monolayer 2D graphene sheet with the gapless, but parabolic, dispersion (massive non-relativistic particles) in bilayer graphene<sup>34</sup>.

Furthermore, our NEGF conductance calculations for segmented zigzag GNRs exhibited Fabry-Pérot oscillatory patterns, with the spacing between peaks behaving as  $1/L^2$  (where  $L$  is the length of the GNR segment). This differs from the (photon-like) FP pattern found for the metallic case of armchair GNRs where the spacing between peaks in the oscillatory conductance varies as  $1/L$  (characteristic of massless particles with linear energy-momentum dispersion, e.g. photons), which were studied<sup>21</sup> by Fabry and Pérot. This directly suggests that the zigzag GNRs can be described by a non-relativistic limit of the Dirac equation with a sufficiently large mass (i.e. by the Schrödinger equation).

Focusing on the intrinsic properties of the graphene lattice, originating from the topology of the honeycomb network, and using a NEGF approach, we have studied here the transport properties of atomically precise segmented armchair and zigzag graphene nanoribbons, with segments of different widths. Mixed armchair-zigzag junctions (with segments of different widths) have also been discussed.

The electronic conductance is found to exhibit Fabry-Pérot oscillations, or resonant tunneling, associated with partial confinement and formation of a quantum box (resonant cavity) in the junction. The Fabry-Pérot oscillations occur for junctions that are strongly coupled to the leads (open system), whereas the resonant-tunneling spikes appear for weak lead-junction coupling (closed system). In particular, with regard to the FP interference patterns, three distinct categories were identified (see the Introduction), with only one of them having the characteristics of the optical<sup>21</sup> FP pattern corresponding to massless graphene electrons exhibiting equal spacings between neighboring peaks.

Perfect quantized-conductance at steps were found only for uniform GNRs. In the absence of extraneous factors, like disorder, in our theoretical model, the deviations from the perfect quantized-

conductance steps were unexpected. However, this aforementioned behavior obtained through TB-NEGF calculations is well accounted for by a 1D continuum fermionic Dirac-Fabry-Pérot interference theory (see Methods). This approach employs an effective position-dependent mass term in the Dirac Hamiltonian to absorb the finite-width (valence-to-conduction) gap in armchair nanoribbon segments, as well as the barriers at the interfaces between nanoribbon segments forming a junction. For zigzag nanoribbon segments the mass term in the Dirac equation reflects the nonrelativistic Schrödinger-type behavior of the excitations. We emphasize that the mass in zigzag-terminated GNR segments is much larger than the mass in semiconducting armchair-terminated GNR segments. Furthermore in the zigzag GNR segments (which are always characterized by a vanishing valence-to-conduction energy gap), the mass corresponds simply to the carrier mass. In the armchair GNR segments, the carrier mass endows (in addition) the segment with a valence-to-conduction energy gap, according to Einstein’s relativistic energy relation [see Eq. (1)].

We observe here that the Dirac Fabry-Pérot masses that we find to yield agreement with the TB conductance spectra agree well with those obtained through Density Functional Theory (DFT) calculations<sup>4</sup> where the energy gap  $\Delta/2 = \mathcal{M}v_F^2$  for armchair GNRs versus width has been determined. For example, for  $\mathcal{N}^W = 5$  and  $\mathcal{N}^W = 7$ , Eq. (1) in Ref. 4 yields  $\Delta/2 = 0.06 t$  and  $0.28 t$ , respectively. These DFT values agree well with the DFP values of  $0.05 t$  (central segment) and  $0.28 t$  (leads) given in the caption of Fig. 4, where the H-passivation effect according to the DFT was incorporated in the TB description.

The above findings point to a most fundamental underlying physics, namely that the topology of disruptions of the regular honeycomb lattice (e.g., variable width segments, corners, edges) generate a scalar-potential field (position-dependent mass, identified also as a Higgs-type field<sup>28,35</sup>), which when integrated into a generalized Dirac equation for the electrons provides a unifying framework for the analysis of transport processes through graphene constrictions and segmented junctions.

With growing activities and further improvements in the areas of bottom-up fabrication and manipulation of atomically precise<sup>8–12</sup> graphene nanostructures and the anticipated measurement of conductance through them, the above findings could serve as impetus and implements aiding the design and interpretation of future experiments.

## Methods

**Dirac-Fabry-Pérot model.** The energy of a relativistic fermion (with one-dimensional momentum  $p_x$ ) is given by the Einstein relation

$E = \sqrt{(p_x v_F)^2 + (\mathcal{M}v_F^2)^2}$ , where  $\mathcal{M}$  is the rest mass and  $v_F$  is the Fermi velocity of graphene. (In a uniform armchair graphene nanoribbon, the mass parameter is related to the particle-hole energy gap,  $\Delta$ , as  $\mathcal{M} = \Delta/(2v_F^2)$ .) Following the relativistic quantum-field Lagrangian formalism, the mass  $\mathcal{M}$  is replaced by a position-dependent scalar Higgs field  $\phi(x) \equiv m(x)v_F^2$ , to which the relativistic fermionic field  $\Psi(x)$  couples through the Yukawa Lagrangian<sup>35</sup>  $\mathcal{L}_Y = -\phi\Psi^\dagger\beta\Psi$  ( $\beta$  being a Pauli matrix). For  $\phi(x) \equiv \phi_0$  (constant)  $\mathcal{M}v_F^2 = \phi_0$ , and the massive fermion Dirac theory is recovered. The Dirac equation is generalized as (here we do not consider applied electric or magnetic fields)

$$[E - V(x)]\Psi + i\hbar v_F \alpha \frac{\partial \Psi}{\partial x} - \beta \phi(x)\Psi = 0. \quad (8)$$

In one dimension, the fermion field is a two-component spinor  $\Psi = (\psi_u, \psi_l)^T$ ;  $u$  and  $l$  stand, respectively, for the upper and lower component and  $\alpha$  and  $\beta$  can be any two of the three Pauli matrices. Note that the Higgs field enters in the last term of Eq. (8).  $V(x)$  in the first term is the usual electrostatic potential, which is inoperative due to the Klein phenomenon<sup>26,27</sup> and thus is set to zero for the case of the armchair nanoribbons (where the excitations are relativistic). The generalized Dirac Eq. (8) is used in the construction of the transfer matrices of the Dirac-Fabry-Pérot model described below.



The building block of the DFP model is a  $2 \times 2$  wave-function matrix  $\Omega$  formed by the components of two independent spinor solutions (at a point  $x$ ) of the one-dimensional, first-order generalized Dirac equation [see Eq. (3) in the main paper].  $\Omega$  plays<sup>36</sup> the role of the Wronskian matrix  $W$  used in the second-order nonrelativistic Kronig-Penney model. Following Ref. 36 and generalizing to  $N$  regions, we use the simple form of  $\Omega$  in the Dirac representation ( $\alpha = \sigma_1$ ,  $\beta = \sigma_3$ ), namely

$$\Omega_K(x) = \begin{pmatrix} e^{iKx} & e^{-iKx} \\ \Lambda e^{iKx} & -\Lambda e^{-iKx} \end{pmatrix}, \quad (9)$$

where

$$K^2 = \frac{(E-V)^2 - m^2 v_F^4}{\hbar^2 v_F^2}, \quad \Lambda = \frac{\hbar v_F K}{E-V + m v_F^2}. \quad (10)$$

The transfer matrix for a given region (extending between two matching points  $x_1$  and  $x_2$  specifying the potential steps  $m_i^{(p)}$ ) is the product  $\mathbf{M}_K(x_1, x_2) = \Omega_K(x_2) \Omega_K^{-1}(x_1)$ ; this latter matrix depends only on the width  $x_2 - x_1$  of the region, and not separately on  $x_1$  or  $x_2$ .

The transfer matrix corresponding to a series of  $N$  regions can be formed<sup>35</sup> as the product

$$\mathbf{t}_{1,N+1} = \prod_{i=1,N} \mathbf{M}_{K_i}(x_i, x_{i+1}), \quad (11)$$

where  $|x_{i+1} - x_i| = L_i$  is the width of the  $i$ th region [with  $(m, V, K, \Lambda) \rightarrow (m_p, V_p, V_b, \Lambda_i)$ ]. The transfer matrix associated with the transmission of a free fermion of mass  $\mathcal{M}$  (incoming from the right) through the multiple mass barriers is the product

$$T(E) = \Omega_K^{-1}(x_{N+1}) \mathbf{t}_{1,N+1} \Omega_K(x_1), \quad (12)$$

with  $k = \sqrt{(E-V)^2 - \mathcal{M}^2 v_F^4} / \hbar v_F$ ;  $|E-V| \geq \mathcal{M} v_F^2$ ; for armchair leads  $V = 0$ , while for zigzag leads  $V = \mp \mathcal{M} v_F^2$ . Naturally, in the case of metallic armchair leads,  $k = E / (\hbar v_F)$ , since  $\mathcal{M} = 0$ .

Then the transmission coefficient  $T$  is

$$T = \frac{1}{|T_{22}|^2}, \quad (13)$$

while the reflection coefficient is given by

$$R = \left| \frac{T_{12}}{T_{22}} \right|^2. \quad (14)$$

At zero temperature, the conductance is given by  $G = (2e^2/h)T$ ;  $T$  is the transmission coefficient in Eq. (13).

**TB-NEGF formalism.** To describe the properties of graphene nanostructures in the tight-binding approximation, we use the hamiltonian

$$H_{\text{TB}} = -t \sum_{\langle ij \rangle} c_i^\dagger c_j + h.c., \quad (15)$$

with  $\langle \rangle$  indicating summation over the nearest-neighbor sites  $i, j$ .  $t = 2.7$  eV is the hopping parameter of two-dimensional graphene.

To calculate the TB-NEGF transmission coefficients, the Hamiltonian (15) is employed in conjunction with the well known transport formalism which is based on the nonequilibrium Green's functions<sup>14</sup>.

According to the Landauer theory, the linear conductance is  $G(E) = (2e^2/h)T(E)$ , where the transmission coefficient is calculated as  $T(E) = \text{Tr}[\Gamma_L G^r \Gamma_R G^{\dagger}]$ . The Green's function  $G(E)$  is given by

$$G(E) = (E + i\eta - H_{\text{TB}}^{\text{dev}} - \Sigma_L - \Sigma_R)^{-1}, \quad (16)$$

with  $H_{\text{TB}}^{\text{dev}}$  being the Hamiltonian of the isolated device (junction without the leads).

The self-energies  $\Sigma_{L(R)}$  are given by  $\Sigma_{L(R)} = \tau_{L(R)} [E + i\eta - H_{\text{TB}}^{L(R)}]^{-1} \tau_{L(R)}^\dagger$ , where the hopping matrices  $\tau_{L(R)}$  describe the left (right) device-to-lead coupling, and  $H_{\text{TB}}^{L(R)}$  is the Hamiltonian of the semi-infinite left (right) lead. The broadening matrices are given by  $\Gamma_{L(R)} = i[\Sigma_{L(R)} - \Sigma_{L(R)}^\dagger]$ .

- Novoselov, K. S. *et al.* Electric field effect in atomically thin carbon films. *Science* **306**, 666 (2004).
- Raza, H. Editor, *Graphene Nanoelectronics: Metrology, Synthesis, Properties and Applications*, (Springer, New York, 2012).
- Nakada, K., Fujita, M., Dresselhaus, G. & Dresselhaus, M. S. Edge state in graphene ribbons: Nanometer size effect and edge shape dependence. *Phys. Rev. B* **54**, 17954 (1996).

- Son, Y. W., Cohen, M. L. & Louie, S. G. Energy Gaps in graphene nanoribbons. *Phys. Rev. Lett.* **97**, 216803 (2006).
- Wang, Z. F. *et al.* Tuning the electronic structure of graphene nanoribbons through chemical edge modification: A theoretical study. *Phys. Rev. B* **75**, 113406 (2007).
- Barone, V., Hod, O. & Scuseria, G. E. Electronic structure and stability of semiconducting graphene nanoribbons. *Nano Lett.* **6**, 2748 (2006).
- Wakabayashi, K., Sasaki, K., Nakanishi, T. & Enoki, T. Electronic states of graphene nanoribbons and analytical solutions. *Sci. Technol. Adv. Mater.* **11**, 054504 (2010), and references therein.
- Cai, J. M. *et al.* Atomically precise bottom-up fabrication of graphene nanoribbons. *Nature* **466**, 470 (2010).
- Huang, H. Spatially resolved electronic structures of atomically precise armchair graphene nanoribbons. *Sci. Rep.* **2**, 983 (2012).
- Van der Lit, J. *et al.* Suppression of electron-vibron coupling in graphene nanoribbons contacted via a single atom. *Nat. Commun.* **4**, 2023 (2013).
- Narita, A. *et al.* Synthesis of structurally well-defined and liquid-phase-processable graphene nanoribbons. *Nat. Chem.* **6**, 126 (2014).
- Vo, T. H. *et al.* Large-scale solution synthesis of narrow graphene nanoribbons. *Nat. Commun.* **5**, 3189 (2014).
- Blankenburg, S. *et al.* Intraribbon heterojunction formation in ultranarrow graphene nanoribbons. *ACS Nano* **6**, 2020 (2012).
- Datta, S. *Quantum Transport: Atom to Transistor*, (Cambridge University Press, Cambridge, 2005).
- van Houten, H., Beenakker, C. W. J., Williamson, J. G., Broekaart, M. E. I. & van Loosdrecht, P. H. M. Coherent electron focusing with quantum point contacts in a two-dimensional electron gas. *Phys. Rev. B* **39**, 8556 (1989).
- Ji, Y. *et al.* An electronic Mach-Zehnder interferometer. *Nature* **422**, 415 (2003).
- vanWees, B. J. *et al.* Quantized conductance of point contacts in a two-dimensional electron gas. *Phys. Rev. Lett.* **60**, 848 (1988).
- Pascual, J. I. *et al.* Properties of metallic nanowires: from conductance quantization to localization. *Science* **267**, 1793 (1995).
- Liang, W. *et al.* Fabry-Pérot interference in a nanotube electron waveguide. *Nature* **411**, 665 (2001).
- Tombros, N. *et al.* Quantized conductance of a suspended graphene nanoconstriction. *Nat. Phys.* **7**, 697 (2011).
- Lipson, S. G., Lipson, H. & Tannhauser, D. S. *Optical Physics* (Cambridge Univ. Press, London, 1995, 3rd ed.) p. 248.
- Lu, W., Xiang, J., Timko, B. P., Wu, Y. & Lieber, C. M. One-dimensional hole gas in germanium/silicon nanowire heterostructures. *Proc. Nat. Acad. Sci.* **102**, 10046 (2005).
- Landman, U., Barnett, R. N., Scherbakov, A. G. & Avouris, Ph. Metal-semiconductor nanocontacts: Silicon nanowires. *Phys. Rev. Lett.* **85**, 1958 (2000).
- Rickhaus, P. *et al.* Ballistic interferences in suspended graphene. *Nat. Commun.* **4**, 2342 (2013).
- Alberto, P., Fiolhais, C. & Gil, V. M. S. Relativistic particle in a box. *Eur. J. Phys.* **17**, 19 (1996).
- Katsnelson, M. I., Novoselov, K. S. & Geim, A. K. Chiral tunnelling and the Klein paradox in graphene. *Nature Phys.* **2**, 620 (2006).
- Rodríguez-Vargas, I. *et al.* A comparative study of Klein and non-Klein tunneling structures. *J. App. Phys.* **112**, 073711 (2012).
- Yannouleas, C., Romanovsky, I. & Landman, U. Beyond the constant-mass Dirac physics: Solitons, charge fractionization, and the emergence of topological insulators in graphene rings. *Phys. Rev. B* **89**, 035432 (2014).
- López-Villanueva, J. A., Melchor, I., Cartujo, P. & Carceller, J. E. Modified Schrödinger-equation including nonparabolicity for the study of a two-dimensional electron gas. *Phys. Rev. B* **48**, 1626 (1993).
- Brey, L. & Fertig, H. A. Electronic states of graphene nanoribbons studied with the Dirac equation. *Phys. Rev. B* **73**, 235411 (2006).
- Zheng, H. *et al.* Analytical study of electronic structure in armchair graphene nanoribbons. *Phys. Rev. B* **75**, 165414 (2007).
- Kivelson, S. & Chapman, O. L. Polyacene and a new class of quasi-one-dimensional conductors. *Phys. Rev.* **28**, 7236 (1983).
- Onipko, A. Spectrum of pi electrons in graphene as an alternant macromolecule. *Phys. Rev. B* **78**, 245412 (2008).
- McCann, A. & Koshino, M. The electronic properties of bilayer graphene. *Rep. Prog. Phys.* **76**, 056503 (2013).
- Romanovsky, I., Yannouleas, C. & Landman, U. Topological effects and particle physics analogies beyond the massless Dirac-Weyl fermion in graphene nanorings. *Phys. Rev. B* **87**, 165431 (2013).
- McKellar, B. H. J. & Stephenson, Jr, G. J. Relativistic quarks in one-dimensional periodic structures. *Phys. Rev. C* **35**, 2262 (1987).

## Acknowledgments

This work was supported by a grant from the Office of Basic Energy Sciences of the US Department of Energy under Contract No. FG05-86ER45234. Computations were made at the GATECH Center for Computational Materials Science.



## Author contributions

I.R. and C.Y. performed the computations. C.Y., I.R. and U.L. analyzed the results. C.Y. and U.L. wrote the manuscript.

## Additional information

**Competing financial interests:** The authors declare no competing financial interests.

**How to cite this article:** Yannouleas, C., Romanovsky, I. & Landman, U. Interplay of relativistic and nonrelativistic transport in atomically precise segmented graphene nanoribbons. *Sci. Rep.* 5, 7893; DOI:10.1038/srep07893 (2015).



This work is licensed under a Creative Commons Attribution-NonCommercial-NoDerivs 4.0 International License. The images or other third party material in this article are included in the article's Creative Commons license, unless indicated otherwise in the credit line; if the material is not included under the Creative Commons license, users will need to obtain permission from the license holder in order to reproduce the material. To view a copy of this license, visit <http://creativecommons.org/licenses/by-nc-nd/4.0/>